J. Fluid Mech. (1992), *vol.* 235, *pp.* 325–348
Printed in Great Britain

Rayleigh–Bénard convection in a small box: spatial features and thermal dependence of the velocity field

By M. P. ARROYO[1] AND J. M. SAVIRÓN[2]

[1] Dipartimento Física Aplicada

[2] Dipartimento Ciencia y Tecnología de Materiales y Fluídos,
Facultad de Ciencias, Ciudad Universitaria, 50009-Zaragoza, Spain

(Received 13 September 1989 and in revised form 9 August 1991

An experimental study of the spatial features of Rayleigh–Bénard convection in a small box is presented. Experiments are carried out in a rectangular cell (aspect ratios $\Gamma_x = 2.03$, $\Gamma_y = 1.19$) filled with silicone oil (Prandtl number, $Pr = 130$) for different Rayleigh numbers, Ra (up to $Ra = 75\,Ra_c$, $\mathrm{Ra_c}1707$). The basic structure of the flow field for this range of Ra consists of two rolls with their axes parallel to the shorter horizontal side. Both senses of rotation for the rolls are observed, corresponding to the two branches of the bifurcation. Particle image velocimetry, with a 5 mW He–Ne laser as the illuminating source, is used to measure the velocity field in the midplane of the cell. From it the vorticity field (out of plane component) and two-dimensional streamlines are calculated. The flow has been measured to be three-dimensional, even for very low Ra, owing to the sidewall influence. The spatial features of the flow are shown to be dependent on both Ra and the sense of rotation of the rolls. Finally, a Fourier analysis of the velocity field is presented. The spatial and thermal dependences of the different Fourier terms are reported. The velocity field, in a first-order approximation, is quantitatively described.

1. Introduction

Different spatial configurations can be obtained in a Rayleigh–Bénard convective flow depending on the geometrical characteristics of the fluid layer, the Prandtl number of the fluid and the Rayleigh number. This paper deals with high-Prandtl-number fluids contained in a three-dimensional rectangular box. The shape of the box is specified by the aspect ratios $\Gamma_x = L_x/L_z$ and $\Gamma_y = L_y/L_z$, where L_x, L_y are horizontal dimensions and L_z is its height.

When aspect ratios are large enough, sidewall effects can be neglected and the fluid layer can be considered infinite in extent. In this case, the convective motion begins at a critical Rayleigh number $Ra_c = 1707$, when the fluid layer is confined above and below by rigid plates of good thermal conductivity (Chandrasekhar 1961). However, in the case of low-aspect-ratio boxes, the influence of sidewalls cannot be neglected. The theoretical treatment is then more difficult and numerical procedures must be used to solve the equations which govern the flow. Sidewalls have a further stabilizing effect on the onset of convective flow owing to the viscous drag which they introduce. It has been shown, theoretically (Davis 1967, 1968) and experimentally (Charlson & Sani 1970; Stork & Muller 1972), that the critical Rayleigh number is higher in small boxes than in large ones. Its value depends on Γ_x and Γ_y but also on

the thermal characteristics of the fluid and sidewalls. A general conclusion is that Ra_c increases when Γ_x, Γ_y or the thermal conductivity of the sidewalls decreases.

Just above Ra_c, the spatial pattern preferred by the flow consists of a series of parallel and straight long rolls with their axes parallel to the shorter side of the box (Davis 1967; Stork & Muller 1972), even if Γ_x and Γ_y are large. The rolls turn clockwise or counterclockwise alternately in space. In theory a given roll can turn in either sense with the same probability, but in practice any small imperfection in the experimental conditions removes the degeneracy. In fact, owing to the thermal characteristics of the sidewalls, the way in which Ra is increased until just above Ra_c (heating from below, cooling from above, doing it quickly or slowly) completely determines the sense of rotation of each roll (Bergé & Dubois 1984).

Most of the experimental work reported in the literature (Busse 1981; Zierep & Oertel 1981; Bergé 1981; Dubois 1981; Gollub, McCarriar & Steinmann 1982) is directed, in a global way, to describing the spatial organization of the different stable patterns and the transitions between them when Ra is modified. But these descriptions do not tell us if the fluid motion is really two-dimensional or if it is exactly the same from one roll to another, for example. This information can only be obtained by measuring a local variable such as the velocity or the temperature perturbation. The most detailed quantitative information about the spatial properties of the flow that has been reported has been obtained from the pointwise velocity measurements, using laser Doppler velocimetry (Dubois & Bergé 1978; Gollub & Benson 1980). In large boxes, only flows at Ra close to Ra_c (up to $Ra \approx 10Ra_c$) have been studied (Dubois & Bergé 1978). This has nevertheless allowed comparisons to be made with a nonlinear theory based on a perturbation approach, developed by Normand, Pomeau & Velarde (1977). In small boxes (Gollub & Benson 1980) there is some information about the spatial structure of a time-dependent flow, but the general relations between the spatial structure and the dynamical behaviour of the flow, and even the spatial structure itself, are still unknown.

In this paper, we present a detailed study of the spatial properties of the Rayleigh–Bénard flow in a small box. The flow in a similar box has been extensively studied by Bergé and Dubois (Dubois 1981; Dubois & Bergé 1981) but they have not considered either the global characteristics or spatial properties of low Ra flows. We have measured the velocity field by particle image velocimetry (§2), which allows simultaneous mapping of the two in-plane components at all the points of a plane. Near the onset of the connection, the pattern consists of two rolls with their axes parallel to the Y-direction. Owing to the sidewalls, the motion must be three-dimensional in the region in which their influence is important. Since it is not known how far it extends into the flow field, we have analysed the central plane ($y = \frac{1}{2}L_y$) which is the farthest from the sidewalls, and where the velocity components parallel to it must be the largest. We have studied flows up to $Ra = 75Ra_c$, where $Ra_c = 1707$. We have also generated the two symmetrical states corresponding to a given Ra in order to compare both spatial structures. Results obtained from this analysis are shown in §3 while the experimental set-up is described in §2.

2. Experimental set-up

2.1. *Rayleigh–Bénard cell (figure 1)*

The cell dimensions are $L_x = 25$ mm, $L_y = 14.6$ mm and $L_z = 12.3$ mm, yielding aspect ratios $\Gamma_x = 2.03$ and $\Gamma_y = 1.19$. The sidewalls are made of 20 mm thick

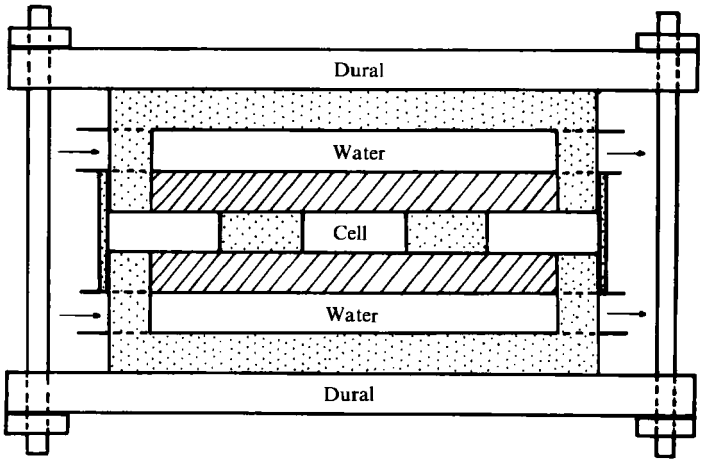

FIGURE 1. Cross-section of the Rayleigh–Bénard cell: ▨, copper; ⬚, Plexiglas.

	Viscosity ν (cm^2/s)	Density ρ (g/cm^3)	Specific heat C_P (cal/g °C)	Thermal conductivity K (cal/cm s °C)	Thermal diffusivity D_t (cm^2/s)	$Pr = \nu/D_t$	Refractive index n
Silicone oil (at 25 °C)	0.1	0.93	0.45	3.2×10^{-4}	7.65×10^{-4}	130	1.399
Plexiglas		1.18	0.35	4.4×10^{-4}	10.76×10^{-4}		1.492
Copper		8.96	0.092	10	1.21		

TABLE 1. Physical properties of the Rayleigh–Bénard cell materials

Plexiglas and the top and bottom of 10 mm thick copper. These materials have been chosen so that the thermal conductivity of the sidewalls is similar to that of the fluid while that of the horizontal boundaries is much higher (table 1). The walls are joined with Canada balsam. Fluid is introduced into the cell by means of a small hole made in one of the upper corners of the Plexiglas frame.

The upper and lower boundaries are kept at the constant temperatures T_0 and $T_0 + \Delta T$ respectively, to within 0.01 °C. This is achieved by circulating water from two independent thermostatic baths. The temperature difference ΔT between the two plates is measured with four Chromel–Alumel thermocouples in series embedded in the copper blocks. The electromotive force produced by this system (163.2 μV/°C) is measured by a digital microvoltmeter with a precision of 1 μV (equivalent to 0.006 °C).

The cell is filled with silicone oil, whose physical properties are shown in table 1. The Prandtl number Pr is high: about 130 at 25 °C. All parameters in table have been taken from the table provided by the manufacturer. The fluid is seeded with 1.1 μm diameter latex particles, which had to be dried and powdered before introducing them into the fluid. The size distribution is 1.1–20 μm.

2.2. *Particle image velocimetry*

The local velocity in the field has been measured by particle image velocimetry, a powerful technique which allows the simultaneous measurement of two components of the velocity in all points of a plane. The technique consists of two steps: (*a*)

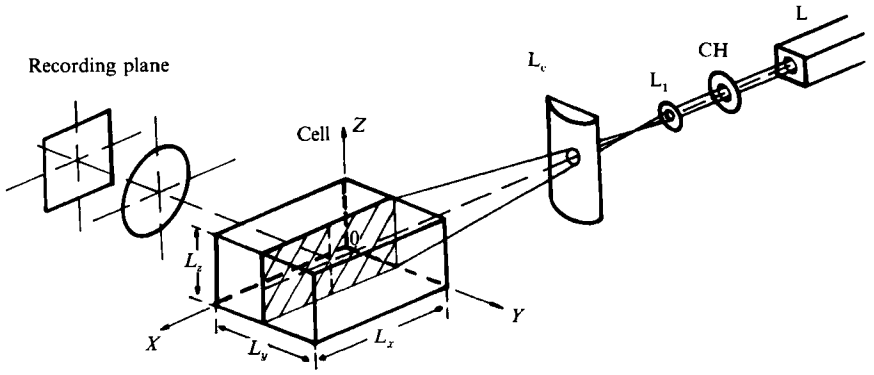

FIGURE 2. Multiple exposure photographic recording system: L, 5 mW He–Ne laser; CH, electromechanical chopper; L_1, *5 microscope objective; L_c, 86-mm focal length cylindrical lens.

recording a multiple exposure photograph of a plane within the flow and (*b*) analysis of the photograph to obtain the velocity field.

The experimental set-up for the first step is shown in figure 2. A sheet of light, with thickness less than 150 μm, is provided by a linearly polarized 5 mW He–Ne laser, shaped with a suitable optical system. An electromechanical chopper, in the form of two blades which are opened and closed, controls the multiple exposures, allowing us to obtain pulses with a minimum duration of 6 ms at time intervals above 100 ms. Both parameters can be changed independently. Time intervals are chosen in order to obtain a maximum displacement between successive images of a few hundred microns. Typically this displacement should be equal to the radius of the interrogation beam used in the analysis process. Exposure times are chosen to be about one tenth of the time intervals.

Light scattered by latex particles seeded in the flow is recorded by a Nikon FM2 camera using a macro 55 mm lens with an extension ring. This system is aberration free even for magnifications as high as unity. Photographs were taken at this magnification with a f/4 aperture, providing a depth of field of 0.6 mm. The system produces particle images ranging from 12 μm to 23 μm diameter. Kodak Technical Pan 2415 film was used because of its very good resolution (about 320 lines/mm) with high sensitivity to red light (about 200 ASA) when developed with D-19 developer. In our set-up, about 20 ms of exposure time is needed to obtain an optical density $D = 1$. Composite images were taken with about ten successive exposures superimposed.

In the second step of particle image velocimetry, several optical methods (Meynart 1983; Pickering & Halliwell 1986–87; Short & Whiffen 1987; Arroyo *et al.* 1988*a*, *b*, *c*) can be used to analyse multiple exposure photographs. In this work we used a point-by-point procedure based on the evaluation of the Young's fringes interference pattern obtained from each pointwise region in the photograph. This method provides accurate measurements of the local in-plane velocity vectors. Our optical processor has already been described elsewhere (Arroyo *et al.* 1988*b*). The photograph is illuminated by a low power He–Ne laser beam of about 0.7 mm diameter and the light intensity distribution (Young's fringes) at the focal plane of a lens placed behind the photograph is observed. Fringes are recorded with a vidicon tube and digitized in a 128 × 128 pixel format with 128 gray levels. A VAX 11/780 computer is used for the digital image processing.

The fringe orientation and frequency are directly related to the direction and the

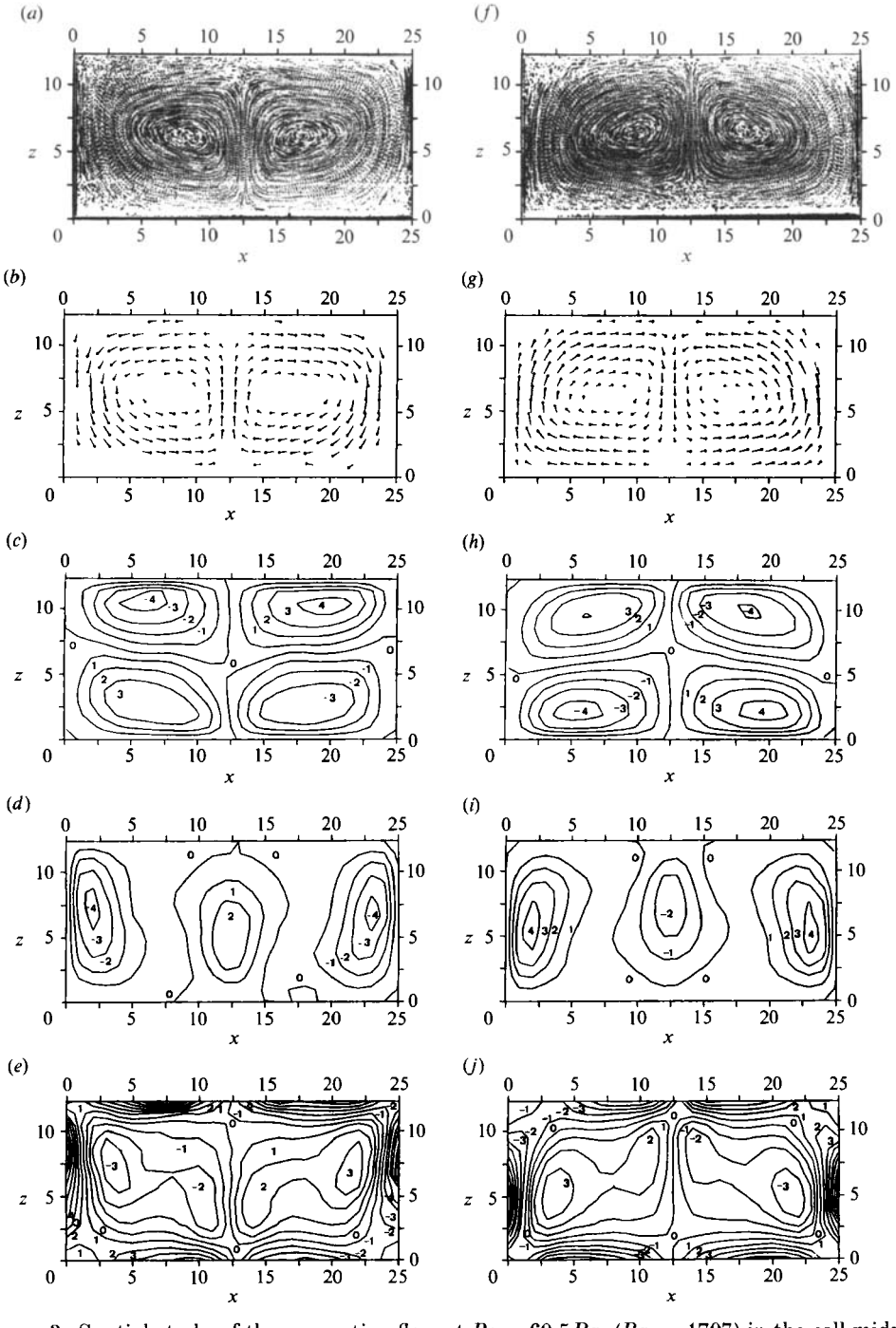

FIGURE 3. Spatial study of the convective flow at $Ra = 60.5Ra_c$ ($Ra_c = 1707$) in the cell midplane ($y = 7.3$ mm) for two equivalent states corresponding to different bifurcation branches obtained by slow heating (images on the left) or fast heating (images on the right-hand size). (a, f) particle image photographs with 10 exposures of 40 ms at 400 ms (a) and 10 exposures of 32 ms at 360 ms (f); (b, g) velocity vector maps from the experimental data. $V_{max} = 788$ μm/s (b) and $V_{max} = 767$ μm/s (g); (c, h) iso-V_x maps. The increments between consecutive lines are $\Delta V_x = 128.2$ μm/s (c) and $\Delta V_x = 125.8$ μm/s (h); (d, i) iso-V_z maps. The increments are $\Delta V_z = 174.6$ μm/s (d) and $\Delta V_z = 170.2$ μm/s (i); (e, j) isovorticity (y-component) maps. The increments are $\Delta\omega = 115.5 \times 10^{-3}$ s^{-1} (e) and $\Delta\omega = 110.2 \times 10^{-3}$ s^{-1} (j).

magnitude of the velocity vector. As a study of the entire flow implies the analysis of many fringe systems, fast and automatic procedures are required. A one-dimensional integration technique with an algorithm which allows the automatic measurement of the fringe orientation is used here (Arroyo *et al.* 1988). The dynamic range of our set-up is about 15.

3. Discussion of the results and conclusions

3.1. *Bifurcation experiments*

It has been observed that the heating routine determines the sense of rotation of the rolls in the convective pattern. In this work the cell is firstly thermostated at 25 °C, a process that starts with the previous stabilization of the upper plate temperature. Later, the bottom plate temperature is raised until a predetermined Ra value is reached. The rate of heating (for Ra close to Ra_c) is the factor that determines the final (steady) rotation sense of the rolls. Low heating rates trigger a rising convective motion of the fluid in the central region of the cell bottom. In contrast, high rates of heating generate a descending fluid flow in that region. These two initial, ascending or descending, streams entirely determine the overall rotation sense of the two rolls. It is remarkable that after the convection is fully developed the sense of rotation of the rolls remains unchangeable, independent of the heating rate.

The main features of the flow in the cell midplane at $Ra = 60.5Ra_c$ for the two bifurcated patterns are presented in figure 3. Particle image photographs (figure 3*a*, *f*) show a very good visualization of the flow. Using these photographs the in-plane velocity fields are measured and displayed as velocity vector maps (figure 3*b*, *g*). The maximum absolute velocity is about 770 μm/s and differs by less than 3% between the two flow patterns, which agrees with our experimental accuracy (2–3%). Data on the two in-plane velocity components (V_x, V_z) and the y-component of the vorticity vector (ω) obtained from the velocity field processing (Arroyo *et al.* 1988*a*) are displayed as isoline maps (figure 3*c–e*, *h–j*). All these maps clearly show the symmetry of the two flows with respect to the transformation $z \to L_z - z$ and $V_z \to -V_z$, which also implies $\omega \to -\omega$.

3.2. *Dependence on Ra*

3.2.1. *Spatial features*

Some experimental results for the flow pattern in the $3.7 < Ra/Ra_c < 75$ range studied are displayed in figures 4–6. Particle image photographs of the cell midplane and the corresponding measured velocity vector map (figure 4) show that rolls are very symmetrical and have a very circular shape, at low Ra values. At higher Ra, the rolls elongate, losing their horizontal symmetry plane. Other spatial features of the flow field are apparent from the iso-V_x and iso-V_z maps (figure 5). These latter change substantially when Ra increases, while the former retain the same essential features even at high Ra values. Moreover, the iso-V_x maps resemble the corresponding two-dimensional convection maps in an infinite box. This indicates that the V_x field is hardly affected by the presence of the walls. The opposite situation is found for the V_z field, which attains a maximum $V_{z\max}$ at the $x = \frac{1}{2}L_x$ plane and negative minima, $V_{z\min}$, very close (2 mm) to the vertical walls. The ratio $V_{z\max}/V_{z\min}$ ranges from -2 to $-2/3$ as Ra is increased.

The isovorticity (y-component) maps (figure 6*a–e*) point out the presence of a zero-vorticity line at a spatial location rather stable against Ra variations. Outside that

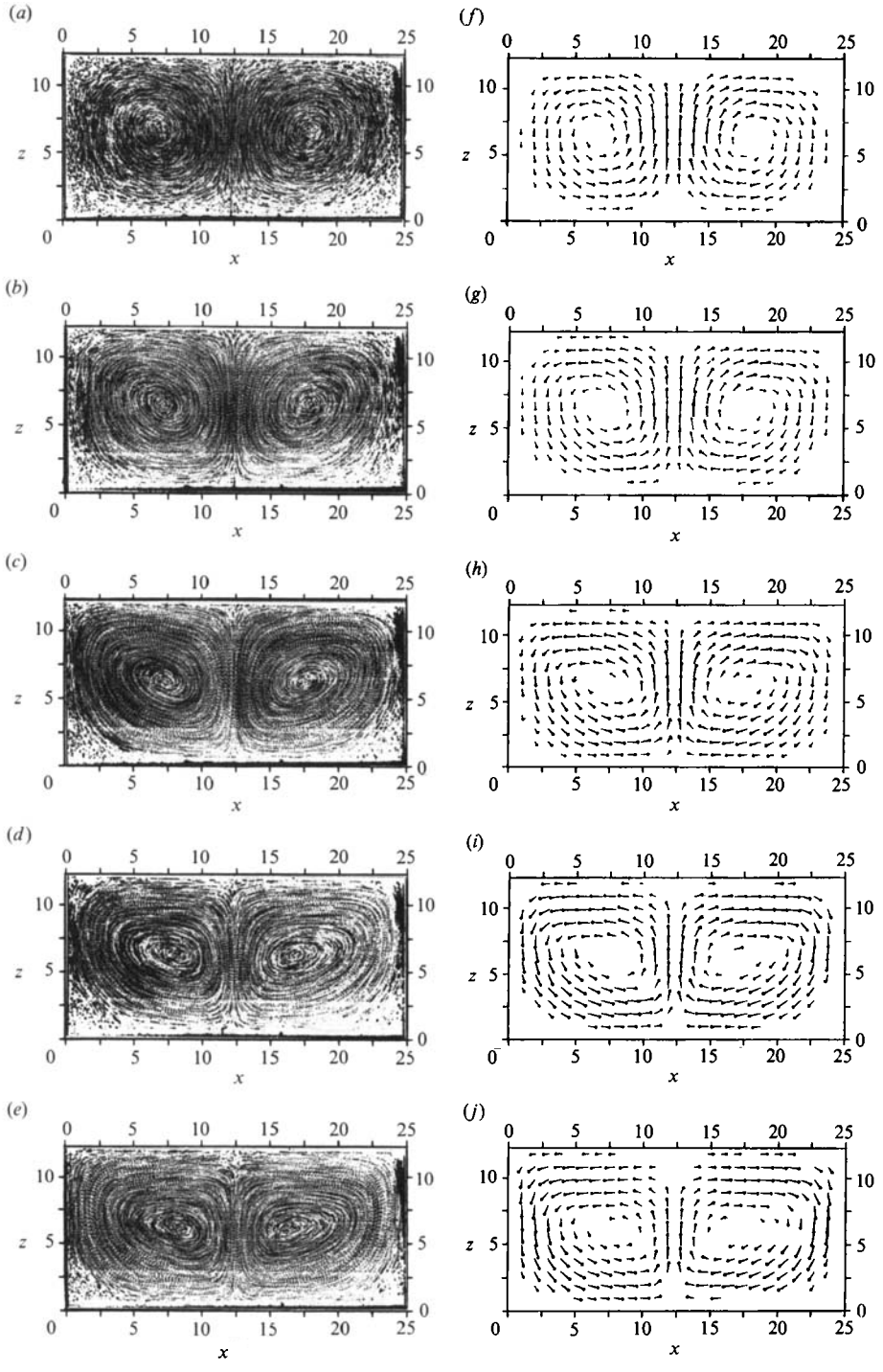

FIGURE 4. Particle image photographs (left-hand side) and corresponding velocity vector maps (right-hand side) of the convective flow at the cell midplane ($y = 7.3$ mm) for different Ra values. (a,f) $Ra = 3.7Ra_c$, Photographs with 7 exposures of 140 ms at 1.4 s (a), $V_{max} = 108$ μm/s (f); (b,g) $Ra = 6.5Ra_c$, 8 exposures of 125 ms at 1.25 s (b), $V_{max} = 202$ μm/s (g); (c,h) $Ra = 13.4Ra_c$, 9 exposures of 100 ms at 1.0 s (c), $V_{max} = 284$ μm/s (h); (d, i) $Ra = 26.2Ra_c$, 10 exposures of 65 ms at 0.64 s (d), $V_{max} = 329$ μm/s (i); (e, j) $Ra = 39.0Ra_c$, 19 exposures of 50 ms at 0.55 s (e), $V_{max} = 489$ μm/s (j) ($Ra_c = 1707$).

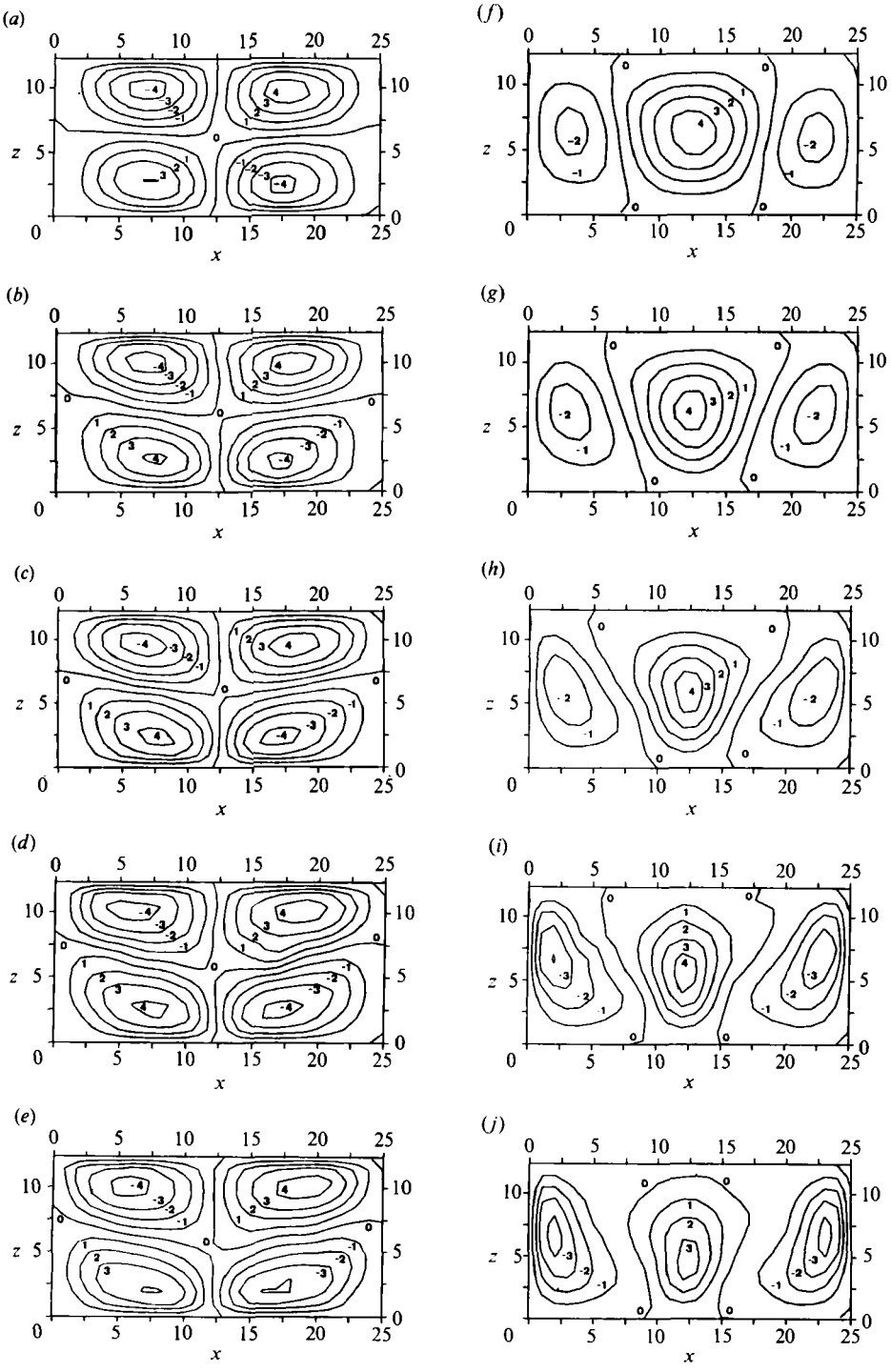

FIGURE 5. Isovelocity component maps for V_x (left-hand side) and V_z (right-hand side) for the same flows shown in figure 4. The increments between consecutive lines are: $\Delta V_x = 15.0\,\mu$m/s (*a*) and $\Delta V_z = 23.9\,\mu$m/s (*f*) for $Ra = 3.7Ra_c$; $\Delta V_x = 30.6\,\mu$m/s (*b*) and $\Delta V_z = 44.9\,\mu$ms/s (*g*) for $Ra = 6.5Ra_c$; $\Delta V_x = 50.6\,\mu$m/s (*c*) and $\Delta V_z = 63.0\,\mu$m/s (*h*) for $Ra = 13.4Ra_c$; $\Delta V_x = 72.0\,\mu$m/s (*d*) and $\Delta V_z = 73.2\,\mu$m/s (*i*) for $Ra = 26.2Ra_c$; $\Delta V_x = 94.3\,\mu$m/s (*e*) and $\Delta V_x = 108.1\,\mu$m/s (*j*) for $Ra = 39.0Ra_c$ ($Ra_c = 1707$).

region, vorticity grows with Ra and the walls induce large vorticity gradients near the boundaries. In contrast, the inner region shows a vorticity field rather less influenced by Ra changes. There are some spatial variations and a redistribution of the areas of maximum vorticity, which increases with Ra as must be expected, but these changes are less dramatic than in the external region.

Finally, simple inspection of the two-dimensional streamlines (figure 6*f–j*) clearly shows the three-dimensional character of the flow pattern, even at low Ra. The spiralling of the streamlines implies that the gradient of the out-of-plane velocity component ($\partial V_y/\partial y$) is non-zero. However, this spiralling of streamlines does not imply that V_y is non-zero. For example, the V_y-field at $Ra = 6.5Ra_c$ has been calculated from the V_x and V_z fields, obtained from the analysis of several parallel planes and application of the continuity equation as described by Arroyo *et al.* (1988*c*). Typical $V_z(y)$ and $V_y(y)$ functions, for a position corresponding to $x = 12$ mm, $z = 6.6$ mm, are shown in figure 7. $V_x(y)$ is not shown as it is very similar to $V_z(y)$. Maximum values for these fields at $Ra = 6.5Ra_c$ are $V_{x\max} = 150$ μm/s, $V_{z\max} = 215$ μm/s and $V_{y\max} = 25$ μm/s. It can be seen that V_y is zero for $y = \frac{1}{2}L_y$ (cell midplane) while $\partial V_y/\partial y$ is quite constant (and different from zero) in an extended region around this cell midplane. The two-dimensional maps for several planes in this central region are very similar (Arroyo *et al.*1988*c*), corresponding to a quite constant $\partial V_y/\partial_y$. However, where V_y takes its maximum absolute values, $\partial V_y/\partial_y$ is zero and the two-dimensional streamlines are more likely to form closed lines. Therefore, we can say that the changes in the spiralling of the two-dimensional streamlines are directly related to changes in $\partial V_y/\partial y$, which may or may not imply changes in the symmetry of the V_y-field.

The three-dimensionality of the flow has also been confirmed, even at $Ra = 3.7\,Ra_c$, by flow rate calculations in the following way. From the mass conservation theorem, and assuming that the density of the fluid is constant, the flow rate, Q, through any closed surface, S, where

$$Q = \oint V \cdot \mathrm{d}\boldsymbol{S}, \tag{1}$$

is zero. If we take a parallelepiped limited by $x = 0$ and $x = L_x$, $z = 0$ and $z = z_o$, $y = y_0 - \frac{1}{2}\Delta y$ and $y = y_0 + \frac{1}{2}\Delta y$ the flow rate, as generalized from (1), may be expressed as

$$Q = \int_0^{L_x}\int_0^{z_0} [V_y(x, y_0+\tfrac{1}{2}\Delta y, z) - V_y(x, y_0-\tfrac{1}{2}\Delta y, z)]\,\mathrm{d}x\,\mathrm{d}z + \int_0^{L_x}\int_{y_0-\frac{1}{2}\Delta y}^{y_0+\frac{1}{2}\Delta y} V_z(x, y, z_0)\,\mathrm{d}x\,\mathrm{d}y = 0. \tag{2}$$

Assuming that Δy is small enough, (2) simplifies to

$$Q = \Delta y\left[\int_0^{L_x}\int_0^{z_0} \partial V_y/\partial y(x, y_0, z)\,\mathrm{d}x\,\mathrm{d}z + \int_0^{L_x} V_z(x, y_0, z_0)\,\mathrm{d}x\right] = 0. \tag{3}$$

From (3) it can be deduced that if the flow is two-dimensional ($\partial V_y/\partial y = 0$ everywhere), the second integral, which will be called flow rate through a Z-line (Q_z), will be zero. If this Q_z is not zero, the flow will be three-dimensional. A relative value for Q_z is defined by

$$Q_z(\%) = 100Q_z/Q_a, \tag{4}$$

where

$$Q_a = \int_0^{L_x} |V_z(x, y_0, z_0)|\,\mathrm{d}x. \tag{5}$$

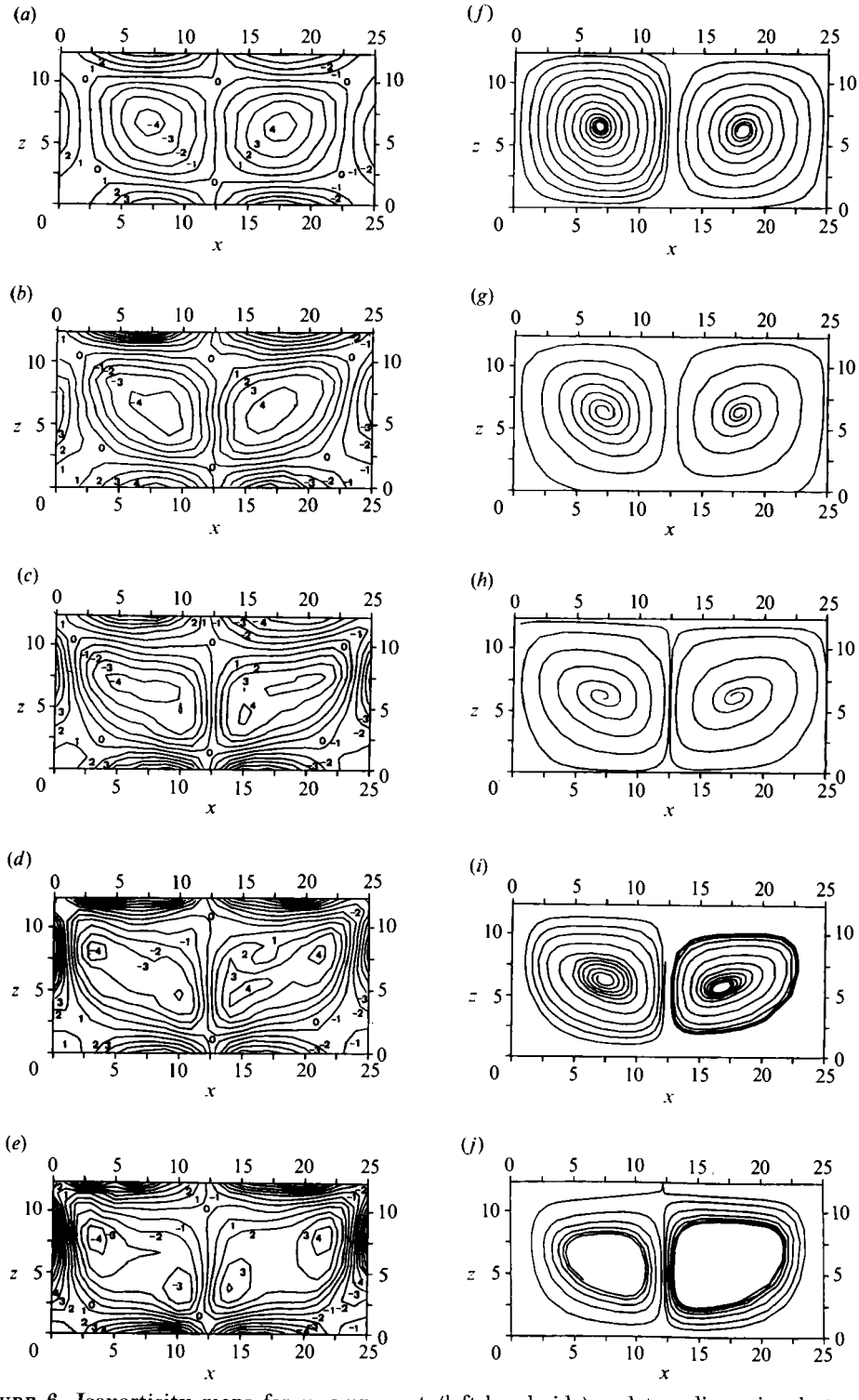

FIGURE 6. Isovorticity maps for y-component (left-hand side) and two-dimensional streamline maps (right-hand side) for the same flows shown in figure 4. The increments between consecutive lines are: $\Delta\omega = 12.5 \times 10^{-3}\ \mathrm{s}^{-1}$ (*a*) for $Ra = 3.7Ra_c$; $\Delta\omega = 20.7 \times 10^{-3}\ \mathrm{s}^{-1}$ (*b*) for $Ra = 6.5Ra_c$; $\Delta\omega = 33.4 \times 10^{-3}\ \mathrm{s}^{-1}$ (*c*) for $Ra = 13.4Ra_c$; $\Delta\omega = 47.3 \times 10^{-3}\ \mathrm{s}^{-1}$ (*d*) for $Ra = 26.2Ra_c$; $\Delta\omega = 62.8 \times 10^{-3}\ \mathrm{s}^{-1}$ (*e*) for $Ra = 39.0Ra_c$ ($Ra_c = 1707$).

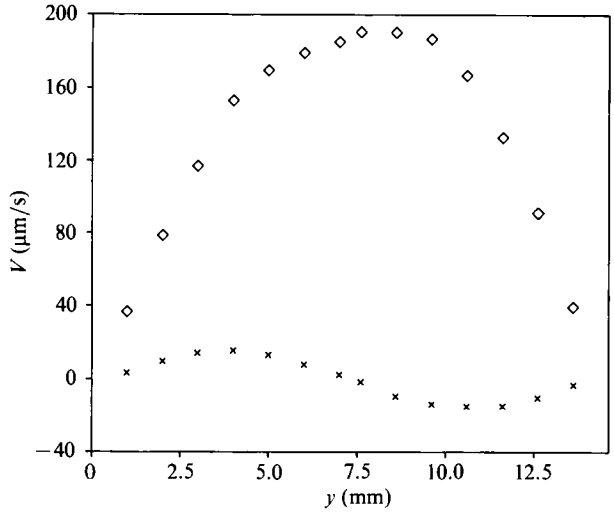

FIGURE 7. Dependence of V_y (×) and V_z (◇) on y for $x = 12$ mm, $z = 6.6$ mm.

We have found that the flow rate $Q_z(\%)$ is not zero even at $Ra = 3.7\,Ra_c$ (table 2). This confirms the three-dimensionality of the flow. No information at all can be obtained from these calculations about the absolute value of either $\partial V_y/\partial y$ or V_y.

With respect to the spatial structure of the flow, our measurements together with some pertinent qualitative observations allow us to deduce that the flow has the same configuration (described by Dubois & Bergé (1981) as a two X roll and no Y roll (2, 0 roll) pattern) over the whole range of Ra analysed here. The main points leading to this conclusion are the following:

(*a*) The visualization of the whole flow, obtained by sweeping the position of the illuminating plane through the whole cell, clearly shows that the $x = \frac{1}{2}L_x$ and $y = \frac{1}{2}L_y$ planes are symmetry planes for the whole range of experiments. This is clearly incompatible with two X rolls and one Y roll (2, 1 roll) patterns.

(*b*) A transition to a two X roll and two Y roll (2, 2 roll) pattern has been observed at $Ra \approx 125\,Ra_c$. As expected, this transition is preceded by a spectacular spatial reorganization of the flow, followed by a very noticeable change in the flow structure. It must be remarked that this reorganization is very apparent even when only the cell midplane is being observed. The spatial features of the flow in the cell midplane for the 2, 2 roll pattern (Arroyo *et al.* 1988*b*) are clearly different from the flow patterns in the present experiments.

(*c*) In the present range of experiments we have not found any visual evidence of a discontinuous change in the spatial features of the flow. Such discontinuities would be indicative of a transition to a different configuration. The changes in the spiralling sense of the two-dimensional streamlines, which are very apparent at $Ra \approx 30\,Ra_c$ (figure 6*i*, *j*) could be indicative of a change of structure. This possibility has been eliminated since a careful examination of the flow around this value of Ra has shown that there is not any discontinuity in the velocity field and that the flow remains symmetric with respect to the $(y = \frac{1}{2}L_y)$ plane.

(*d*) The dependence of V_y and V_z on y (figure 7) shows that the flow has no Y roll since the sign of V_z does not change along Y. This definitely implies that the flow

z(mm)	Q_z(%)
0.95	0.7
1.89	1.6
2.84	6.2
3.78	11.4
4.73	14.9
5.68	18.1
6.62	21.8
7.57	25.3
8.52	28.7
9.46	30.5
10.41	31.2
11.35	37.5

TABLE 2. Flow rates, Q_z(%), trough several Z-lines for $Ra = 3.7Ra_c$

corresponds to the 2, 0 roll pattern. By the present experiments, it can also be said that this 2, 0 roll pattern has a more complex structure than formerly supposed.

3.2.2. *Critical Rayleigh number* Ra'_c

Little information can be found in the literature for predicting the value of the critical Rayleigh number (Ra'_c) in small boxes. Some theoretical calculations on the dependence of Ra'_c with the aspect ration Γ_x have been reported (Oertel 1981; Buhler, Kirchartz & Oertel 1979). These predictions were made for a cell with $Pr = \infty$, perfectly rigid heat conducting sidewalls and horizontal boundaries, and an aspect ratio (Γ_y) fixed at 4. In addition, Frick & Clever (1982) reported calculations for a cell with perfect isolators for sidewalls, taking $Pr = \infty$ and $\Gamma_y = \infty$. However, the experiments of Koster, Ehrard & Muller (1986) demonstrate that Ra'_c in a cell with Plexiglas sidewalls (poor heat conductors), with aspect ratios $\Gamma_x = 0.1$ and $\Gamma_y = 2.76$, and $Pr = 235$ is an order of magnitude greater than the value predicted by Frick & Clever (1982). This discrepancy can be attributed to the different aspect ratio Γ_y. Therefore, a complete analysis of the dependence of Ra'_c with Γ_x, Γ_y, Pr and sidewalls conductivity would be needed for a theoretical prediction of Ra_c value in each particular case. As this analysis is not easily done, it is preferable to measure Ra'_c experimentally in the cell studied.

In this work we have not paid any special attention to the region $Ra \approx Ra'_c$, which would have required a much more precise experimental set-up for temperature control and stabilization. However, measurements were taken which permitted an estimate of Ra'_c to accuracies sufficient for the purpose of the property modelization, which will be described later. Analysis of the dependence of V^2 on Ra/Ra_c (figure 8) at several points where V_x or V_z take their highest absolute value shows that V_z^2 has a nonlinear dependence on Ra/Ra_c which, in turn, depends on the measurement point. In contrast, V_x^2 depends linearly on Ra/Ra_c even for Ra values as high as $39Ra_c$. This reproduces a result first found by Bergé & Dubois (1978) in their study of high-aspect-ratio boxes: $V_{x\max}$ varies as $\epsilon^{\frac{1}{2}}$ for a range of Ra higher than expected. This fact has allowed us to calculate Ra'_c. A linear lsm fitting of $V_x^2 = f(Ra/Ra_c)$ has provided the value $Ra'_c/Ra_c = 2.8 \pm 0.1$ from the extrapolation at $V_x = 0$. The same procedure applied to the lower V_z values leads to the same extrapolated Ra'_c value.

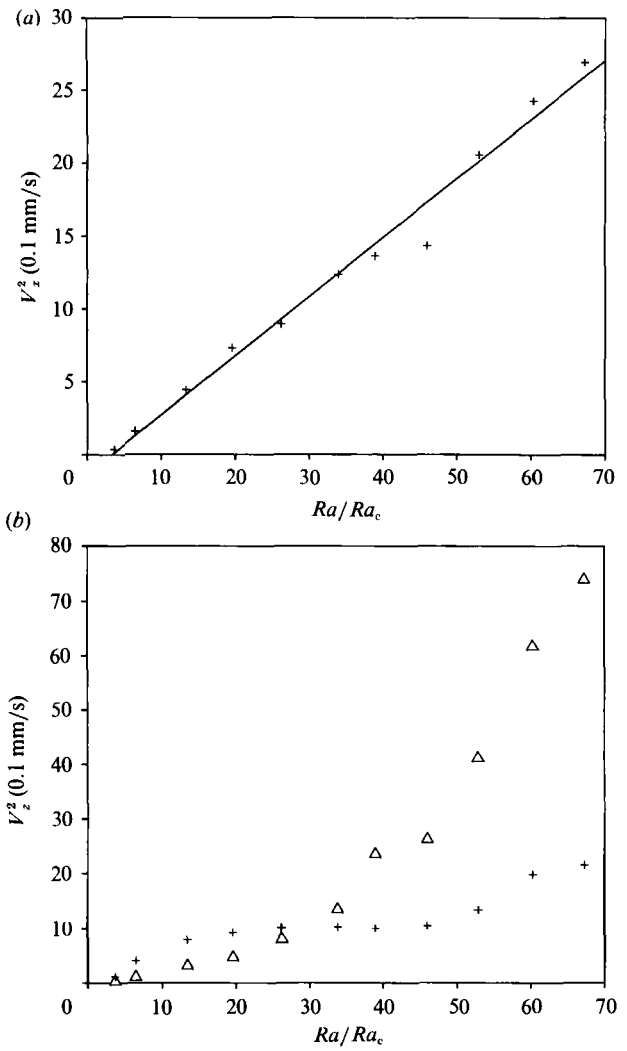

FIGURE 8. Dependence of V^2 on Ra/Ra_c for (*a*) $V_{z\max}$ (in $z = 2.8$ mm, $x = 7$ mm) and (*b*) +, $V_{z\max}$ ($z = 6.6$ mm, $x = 12$ mm); △, $|V_{z\min}|$ ($z = 6.6$ mm, $x = 23$ mm).

3.2.3. *Fourier analysis of the velocity field*

Before presenting our analysis, we first remark that there are no theoretical results for predicting the velocity field in a finite box. The most significant calculations made in that sense for infinite boxes have been reported by Schluter, Lortz & Busse (1965) and Normand *et al.* (1977), with experimental verification provided by Dubois & Bergé (1978). As they present an approach that seems to be the most convenient one for analysing the problem, we will try to follow it as far as possible.

In infinite boxes, the flow is two-dimensional and presents a roll pattern with spatial frequency $f_0 = \frac{1}{2}L_z$. The two velocity components are obtained from the usual expansion in terms of a small parameter ϵ of the form

$$V = \epsilon^{\frac{1}{2}} V_1 + \epsilon V_2 + \epsilon^{\frac{3}{2}} V_3 + \ldots, \tag{6}$$

where $\epsilon = Ra/Ra_c - 1$. This expansion, when restricted to the first terms in $\epsilon (\leqslant \epsilon^{\frac{3}{2}})$ is valid only for low values of ϵ. V_1, V_2, V_3 are found to be harmonic modes of the velocity

(their x-dependence is mainly as $\cos(2\Pi n f_0 x)$ with $n = 1, 2, 3$ respectively) and to have a very definite roll pattern. The procedure used by Dubois & Bergé (1978) for obtaining V_1, V_2, V_3 is the following:

(*a*) Both velocity components (V_x and V_z) are expanded, as functions of X, in a Fourier series with the same frequencies, which are multiples of f_0.

(*b*) The Fourier expansions are performed for several Z-values and for several ϵ-values. The ϵ-dependence of the different terms of the expansions is also obtained.

(*c*) All terms depending on $\epsilon^{\frac{1}{2}}$ are associated with V_1, the terms depending on ϵ with V_2 and the terms depending on $\epsilon^{\frac{3}{2}}$ with V_3.

Before using the same procedure for analysing our measurements, some comments are required regarding its suitability to our problem since the flow is not two-dimensional (as we pointed out earlier) and may not present a clear periodicity along X as the flow has only two rolls, which are affected by the presence of the cell walls.

First of all, we should point out that even though it is always possible to expand any function by a Fourier series, such an expansion is prudent only when the function needs a small number of terms for its equivalent representation. This is true in our case, where V_x and V_z can be expanded as

$$\left.\begin{aligned} V_x &= \sum_{n=1}^{5} V_{xn} \sin(2n\pi x/L_x), \\ V_z &= \sum_{n=1}^{5} V_{zn} \sin((2n-1)\pi x/L_x). \end{aligned}\right\} \tag{7}$$

Owing to the different symmetry exhibited by each function (figure 9), the frequencies of each expansion are also different, being an even multiple of $\frac{1}{2}f_0$ for V_x and an odd multiple for V_z. We should point out that the expression for V_x is similar to the expression in infinite boxes and that only the first two terms are significant for the whole range of ϵ analysed here. All five terms of V_z are important for the highest ϵ, but only two of them are needed at low ϵ. Since the spatial frequencies included in both expansions are different, we cannot properly speak of harmonic modes of the velocity vector field.

Another point to be remarked on is that, owing to the three-dimensionality of the flow, a complete analysis of the velocity field would imply a Fourier expansion on x and y of the three velocity components. No expansion on y can be made as only the $y = \frac{1}{2}L_y$ plane has been analysed for each ϵ. Nevertheless, as V_x and V_z take their maximum value in this plane for the whole range of experiments, their expansion along x is still meaningful.

Finally, we should say something about how the presence of the walls at $x = 0, L_x$ might change the velocity field of the flow and consequently the form of the Fourier expansions. First, we assumed that the sidewall effects could be included in an envelope function which, multiplied by the velocity field in an infinite box, would fit the velocity field in the small box. This envelope, whose analytical form is unknown, should be zero at the walls and increase to its maximum value around the $x = \frac{1}{2}L_x$ position. The Fourier expansion for V_z (equation (7)) suggests that this envelope could be a sinusoidal function with frequency $\frac{1}{2}f_0$. If this is correct, we should find that our measurements at $\epsilon = 0.32$ are predicted well using only the first harmonic mode taken from the infinite box. This would imply that V_{z1} and V_{z2} in (7) should take the same value. This is clearly not the case since we have measured V_{z2} as much larger than V_{z1}. The most definite evidence that this inclusion of the sidewall effects in an envelope function cannot fit our measurements is provided by the fact that V_z goes

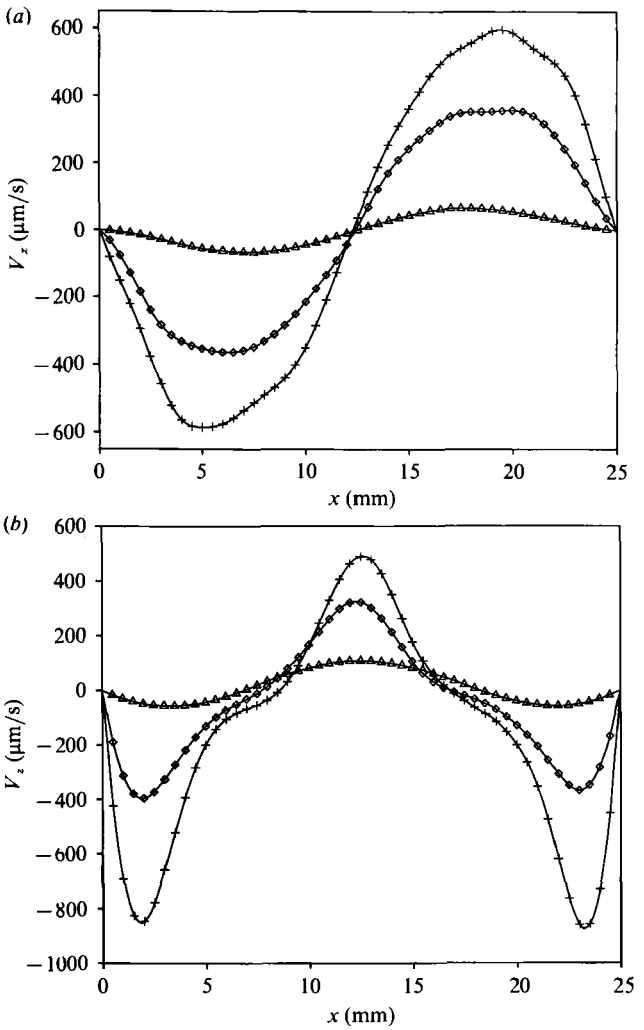

FIGURE 9. Velocity components for three Ra values: △, $\epsilon = 0.32$; ◇, $\epsilon = 11.11$; +, $\epsilon = 23.04$. (*a*) $V_x(x)$, $z = 10.4$ mm, (*b*) $V_z(x)$, $z = 6.6$ mm.

to zero at $x = 0.27L_x$, $0.73L_x$, while it goes to zero at $x = 0.25L_x$, $0.75L_x$ in an infinite box. Whatever expression we take for the envelope, the position of the zero values cannot change. Furthermore, this envelope theory does not fit at all with the Fourier expansion for V_x.

The other possibility we have investigated is whether the effect of the sidewalls on the x-dependence of V_x and V_z is similar to the effect of the horizontal boundaries on the z-dependence of V_x and V_z. For example, it is remarkable that if we take one of the rolls in the infinite box, the dependence of V_x, V_z on x and on z are different. Along x, both have the same fundamental frequency, f_0, but along z, V_z has the same frequency f_0 while the fundamental frequency of V_x is $2f_0$. Furthermore, at small ϵ, where only the fundamental mode is important, $V_x(x)$ and $V_z(x)$ are pure sinusoidal functions while $V_x(z)$ and $V_z(z)$ have a rather complicated analytical expression (Chandrasekhar 1961; Schluter *et al.* 1965), which includes hyperbolic functions. Something very similar happens with $V_x(z)$ and $V_z(z)$ for the second harmonic mode in an infinite box (Normand *et al.*1977; Schluter *et al.* 1965). We have checked that

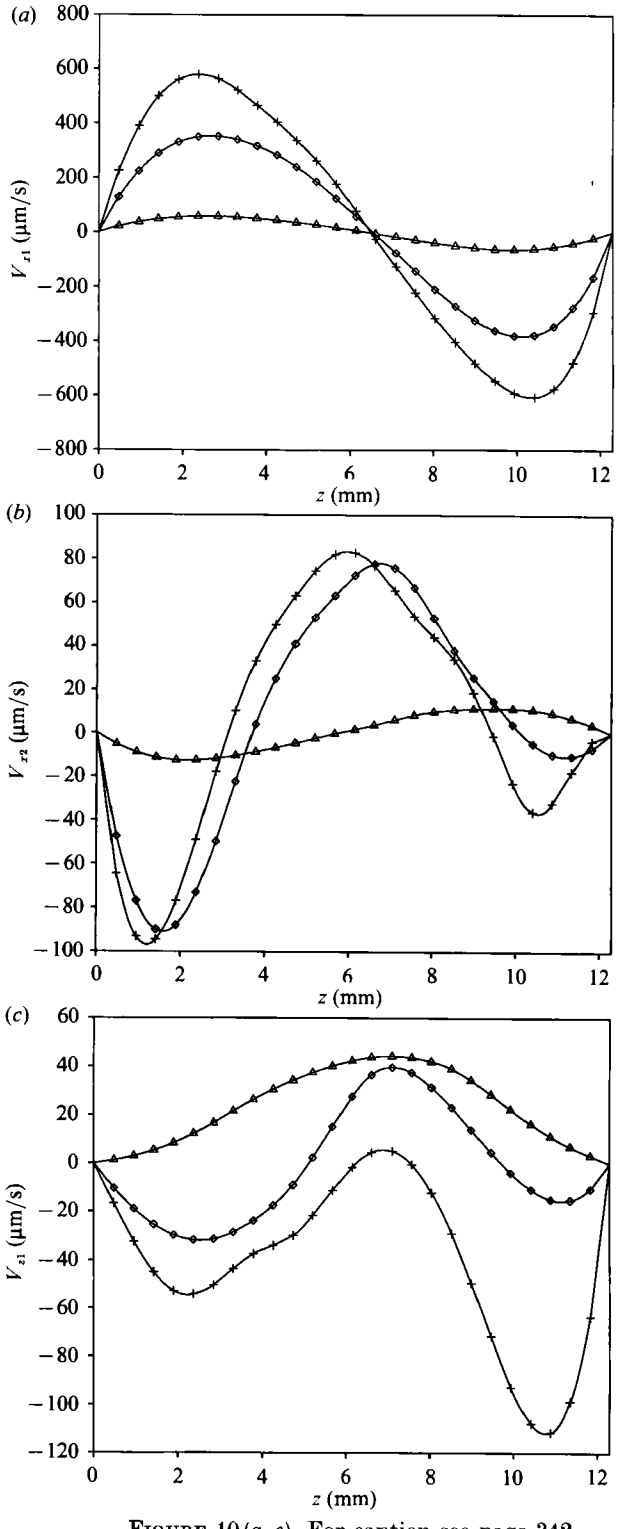

FIGURE 10 (*a–c*). For caption see page 342.

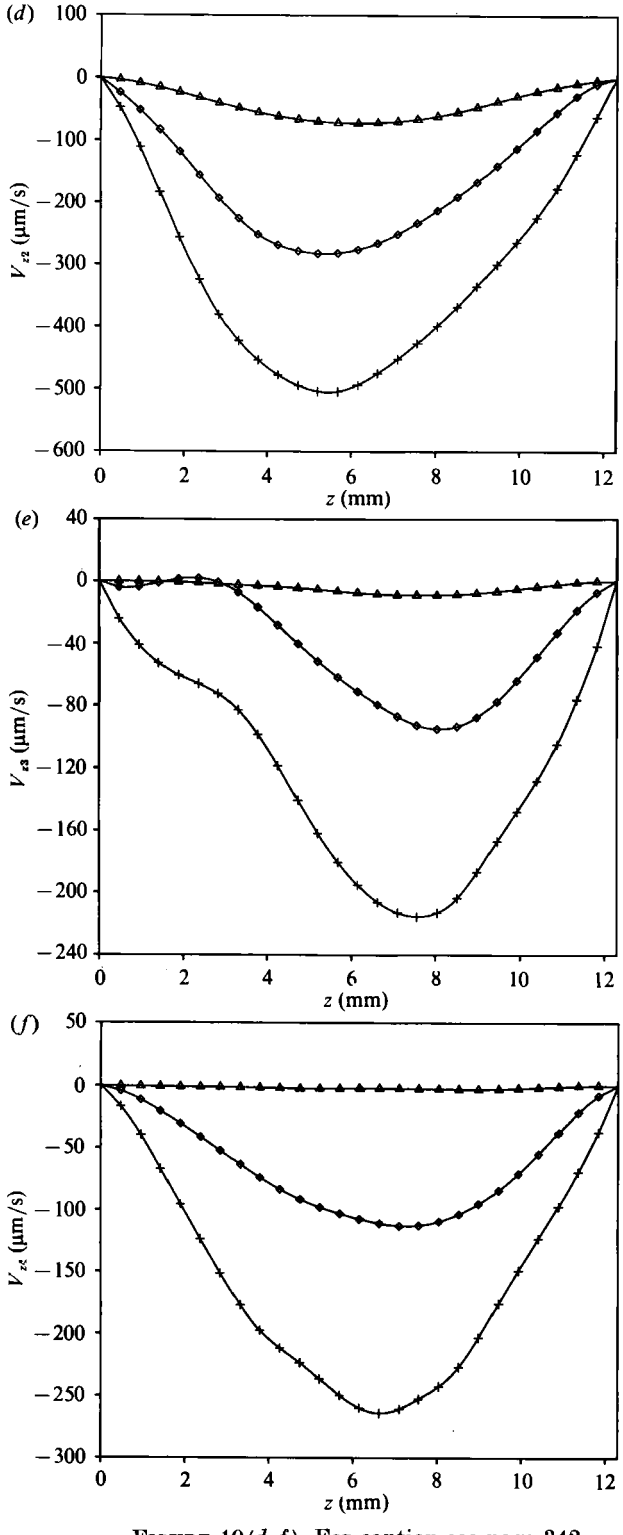

FIGURE 10(*d–f*). For caption see page 342.

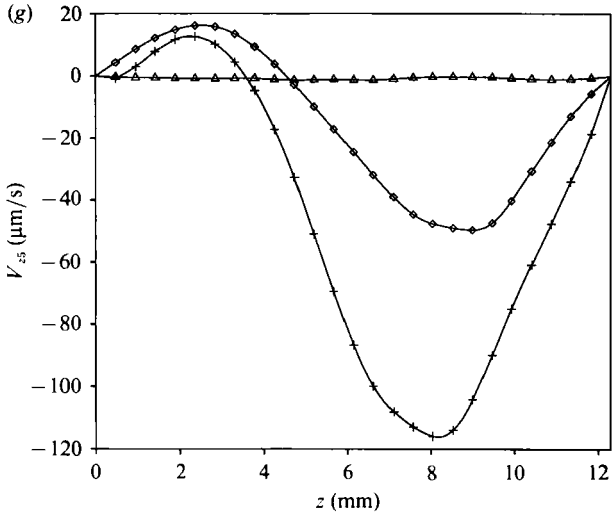

FIGURE 10. Fourier amplitudes for three Ra values: △, $\epsilon = 0.32$; ◇, $\epsilon = 11.11$; +, $\epsilon = 23.04$. (*a*) V_{x1}; (*b*) V_{x2}; (*c*) V_{z1}; (*d*) V_{z2}; (*e*) V_{z3}; (*f*) V_{z4}; (*g*) V_{z5}.

the Fourier expansions which best fit them are similar to (7) (interchanging x by z everywhere) with only two terms in the expansions. The relative values of the different expansion coefficients are similar in both cases. The main differences are found in V_z. They arise from the fact that the second harmonic mode in an infinite box is a two-dimensional flow while our flow is three-dimensional. Now it becomes quite clear that even the 'fundamental' mode V_1 (which is not a true harmonic mode) in a small box is rather complicated. Nevertheless, we will show that it is possible to describe this 'fundamental' mode following the procedure described in the preceding paragraphs. Further theoretical development would be needed for a realistic search of the proper harmonic modes in a small box. However, we think that the results presented here will be useful whenever a theory is available and even they can help in the development of such a theory.

We start by expanding V_x and V_z in a Fourier series following (7) and do so for $z = 0$ to L_z, each 0.5 mm and for each ϵ. The Fourier amplitudes V_{xn} ($n = 1, 2$) and V_{zn} ($n = 1, 5$) are shown in figure 10 (as functions of z) for three different ϵ-values. It can be seen that the form of $V_{x1}(z)$ remains quite unchanged with respect to the variation in ϵ, apart from a slight displacement of its maximum and minimum toward the walls. It resembles the same function in infinite boxes (Normand *et al.* 1977). V_{x2} is always smaller than V_{x1} ($V_{x2\max} \approx \frac{1}{6}V_{x1\max}$) and is quite different from its equivalent in infinite boxes. At low ϵ, V_{x2} is similar to V_{x1}. When ϵ increases, the maximum and minimum of V_{x2} change smoothly and two sublayers appear. From $\epsilon = 11.11$ the sublayers remain practically unchanged, with V_{x2} resembling the V_{x2} in infinite boxes, although it is not as symmetric as it is in infinite boxes.

In the expansion for V_z, V_{z2} is always the most important term. Its z-dependence is similar to the first harmonic dependence in infinite boxes. Its form remains quite unchanged with respect to ϵ, a behaviour similar to that of V_{x1}. V_{z1} is similar to V_{z2} at low ϵ but two sublayers, whose positions remain constant from $\epsilon = 11.11$, appear in the same way as for V_{x2}, as ϵ increases. The ratio $V_{z1\max}/V_{z2\max}$ is now larger at low than at high ϵ. The other three terms for V_z are negligible at low ϵ, but grow larger than V_{z1} at high ϵ.

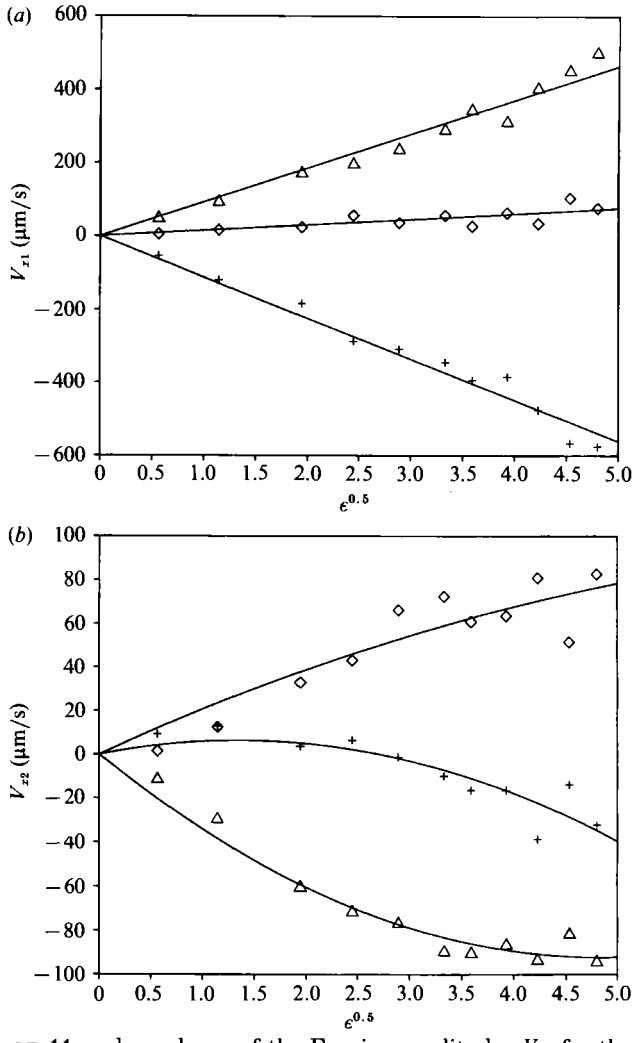

FIGURE 11. ϵ dependence of the Fourier amplitudes V_{xn} for three z-values: △, $z = 1.42$ mm; ◇, $z = 6.15$ mm; +, $z = 10.88$ mm. (*a*) V_{x1}; (*b*)V_{x2}.

We now examine the ϵ-dependence of the expansion coefficients from $z = 0$ to L_z at 0.5 mm intervals. Figures 11 and 12 show this ϵ-dependence for three values ($z = 1.42$, 6.15, 10.88 mm for V_x and $z = 2.37$, 7.10, 10.88 mm for V_z) where either V_{x2} or V_{z1} are maximum or minimum. Also shown is the fitting to powers of $\epsilon^{\frac{1}{2}}$ which produces the best correlation coefficient. The coefficients of the fitting are shown in table 3. It can be seen from figure 11, that V_{x1} shows a clear linear dependence in $\epsilon^{\frac{1}{2}}$. Its maximum value occurs at $z = 2.37$ mm where it can be expressed as $V_{x1} = 115\ \epsilon^{\frac{1}{2}}$ (μm/s). This measured value differs by 6% from the value predicted by the theory for an infinite box, when applied to our small box. The analysis of V_{x2} shows clearly that a term in $\epsilon^{\frac{1}{2}}$ along with a term in ϵ is required for a good fit. This is not surprising as V_{x2} is quite noticeable even at low ϵ. The z-dependences of both terms ($\epsilon^{\frac{1}{2}}$ and ϵ) are similar too, but not as symmetric as those of V_{x1} (figure 10*a*). The maximum value for both $\epsilon^{\frac{1}{2}}$ and ϵ terms occurs at about 2.37 mm where V_{x2} can be expressed as $V_{x2} = -43\,\epsilon^{\frac{1}{2}} + 7\,\epsilon$(μm/s).

The ϵ-dependence of V_{zn} is more complicated to analyse as it does not show a clear

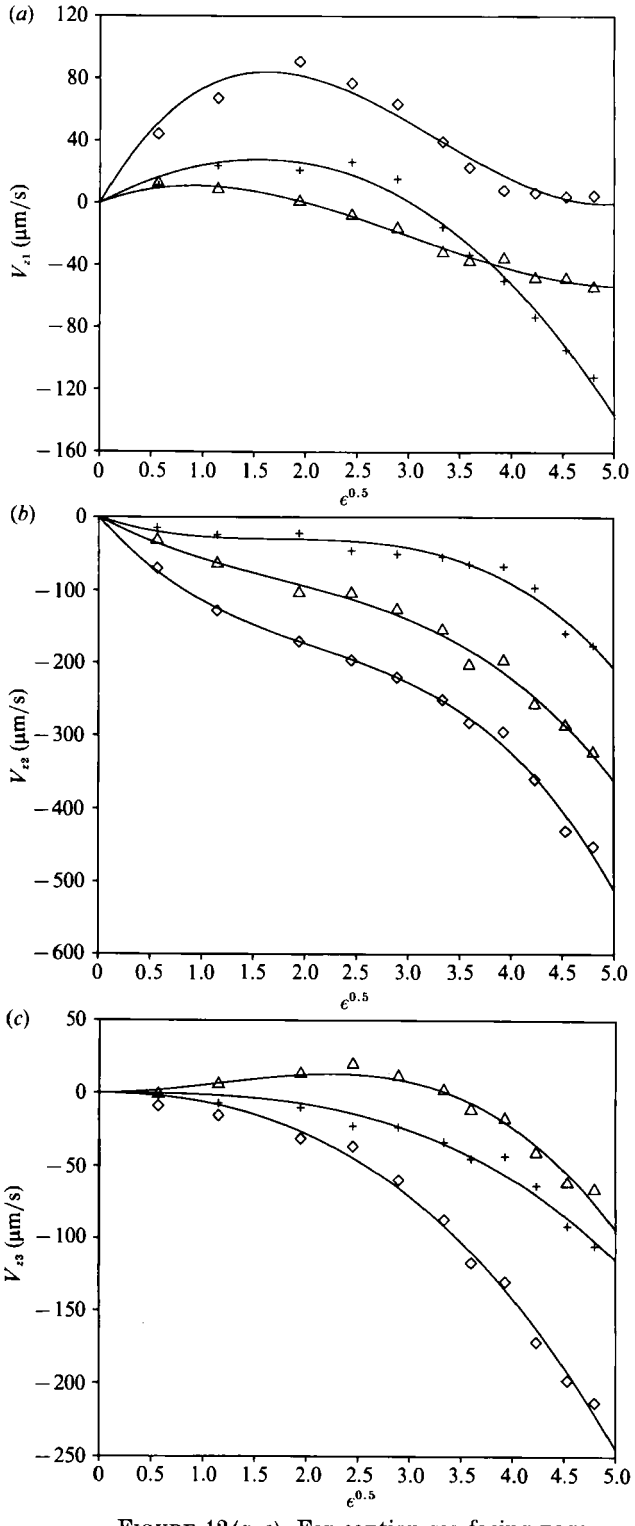

FIGURE 12(*a–c*). For caption see facing page.

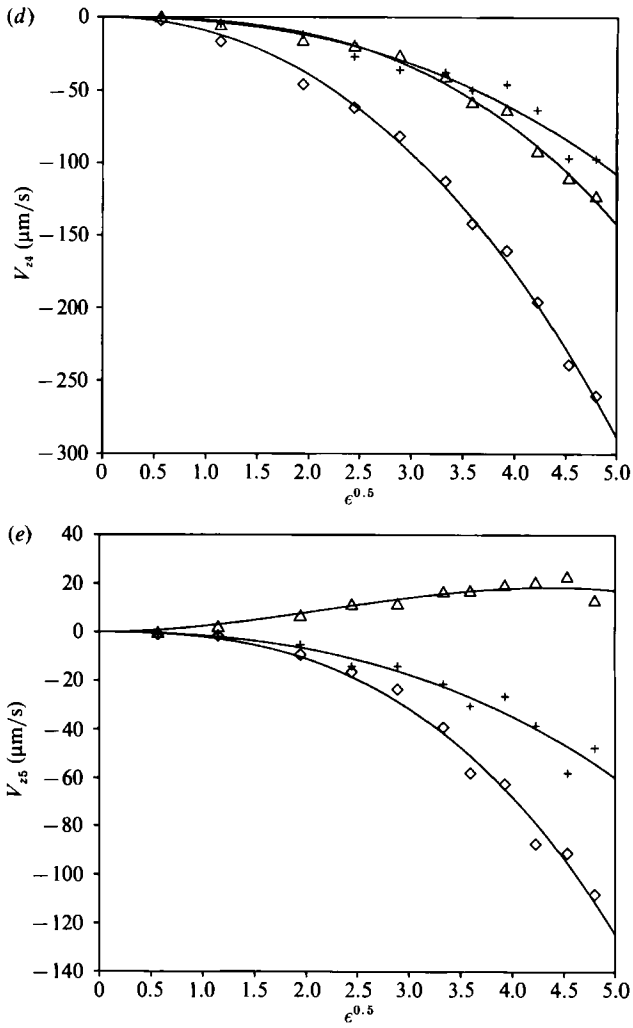

FIGURE 12. ϵ dependence of the Fourier amplitudes V_{zn} for three z-values: △, $z = 2.37$ mm; ◇, $z = 7.10$ mm; +, $z = 10.88$ mm. (*a*) V_{z1}; (*b*) V_{z2}; (*c*) V_{z3}; (*d*) V_{z4}; (*e*) V_{z5}.

dependence. We started by fitting the five coefficients to a third-degree polynomial in $\epsilon^{\frac{1}{2}}$. Then, to simplify the fitting, we tried to remove the small coefficients and check whether the fitting was still correct. In this way, we have checked that not even the strongest coefficient may be fit with only one term. Two (for V_{z3}, V_{z4} and V_{z5}) and even three terms (for V_{z1} and V_{z2}) are needed. With regard to its z-dependence, all the terms (except the ϵ term for V_{z3} and V_{z5}) look like V_{z2} (figure 10*d*). The value of the coefficient for $z = 7.10$ mm then gives the maximum amplitude of each term.

Finally, by putting together the coefficients in $\epsilon^{\frac{1}{2}}$ we may describe the structure of V_1. Its maximum amplitudes may be expressed as

$$\left.\begin{aligned} V_{x\max}(x) &= (115\sin(2\pi x/L_x) - 43\sin(4\pi x/L_x))\,\epsilon^{\frac{1}{2}}, \\ V_{z\max}(x) &= (116\sin(\pi x/L_x) - 157\sin(3\pi x/L_x))\,\epsilon^{\frac{1}{2}}. \end{aligned}\right\} \tag{8}$$

By taking into account all the results concerning the spatial variation of the velocity, we may conclude that V_1 may be accounted for by two rolls inscribed in the whole cell like the rolls depicted in figure 4(*a*).

Term	z(mm)	$\epsilon^{\frac{1}{2}}$	ϵ	$\epsilon^{\frac{3}{2}}$
V_{x1}	1.42	92.8		
(μm/s)	6.15	15.4		
	10.88	−112.1		
V_{x2}	1.42	−38.0	3.91	
(μm/s)	6.15	21.9	−1.25	
	10.88	9.5	−3.48	
V_{z1}	2.37	25.4	−16.1	1.78
(μm/s)	7.10	115.8	−47.3	4.82
	10.88	34.9	−10.1	−0.47
V_{z2}	2.37	−73.9	22.0	−4.34
(μm/s)	7.10	−157.4	51.5	−8.09
	10.88	−47.9	26.3	−5.00
V_{z3}	2.37		7.77	−2.30
(μm/s)	7.10		−4.99	−0.96
	10.88		−0.12	−0.89
V_{z4}	2.37		−0.89	−0.96
(μm/s)	7.10		−8.58	−0.59
	10.88		−2.36	−0.39
V_{z5}	2.37		−2.89	−0.44
(μm/s)	7.10		−1.23	−0.75
	10.88		−1.24	−0.23

TABLE 3. Coefficients of the V_x and V_z expansions

Concerning the structure of V_2 we see that only V_{x2} is necessary for describing the V_x component while all five V_{zn} terms have a contribution in ϵ. Of these, V_{z1} and V_{z2} are the most significant terms, even though the other three cannot be neglected. The different symmetry of the terms in this V_2 mode does not allow its description as a roll pattern.

The structure of V_3 is even more difficult to analyse as no significant value for V_{x3} or the $\epsilon^{\frac{3}{2}}$ dependence of V_{x2} has been found. With respect to V_z, we should remark again that all five terms contribute to V_3

4. Conclusions

A detailed study of the flow in the mid-plane of a Rayleigh–Bénard cell with small aspect ratios ($\Gamma_x = 2$, $\Gamma_y = 1.2$) has been presented. It has been found that the critical Rayleigh number for this cell is $Ra'_c = (2.8 \pm 0.1) Ra_c$, where $Ra_c = 1707$. Flows from $Ra = 0.32 Ra'_c$ approximately up to $25 Ra'_c$, corresponding to the so-called 2, 0 roll pattern, have been studied. The cross-section of the rolls is perfectly circular at very low Ra, but loses symmetry with respect to the horizontal axis at higher Ra. At a given Ra, two different states corresponding to different branches of the bifurcation have been observed. These two states are symmetric with respect to the transformation $z \to L_z - z$, $V_z \to -V_z$ and $\omega \to -\omega$. The flow pattern is three-dimensional even at the lowest Ra analysed ($Ra = 0.32 Ra'_c$). The Fourier expansion of $V_x(x)$ and $V_z(x)$ shows different spatial frequencies, which implies that the complete velocity vector field cannot be described in terms of spatial harmonic modes. The V_x expansion has the same fundamental frequency and similar amplitude and ϵ-dependence as it has in infinite boxes, corresponding to a small sidewall effect on this component. Even so, in the first-order approximation for the velocity field there is an additional small, but non-negligible, contribution of the second term of the Fourier expansion. In contrast,

V_z is more strongly affected by the sidewalls. Again, two terms are needed in the first-order approximation, but now the other expansion terms become comparable quite quickly as ϵ increases. The velocity field in this first-order approximation reproduces quite well the measurements at low *Ra* and can be accounted for by two rolls inscribed in the whole cell. The second- and third-order approximations cannot be easily described as roll patterns.

The authors would like to thank Professor M. Quintanilla for many helpful discussions on the particle image velocimetry and T. Yonte for her experimental assistance.

REFERENCES

ARROYO, M. P., YONTE, T., QUINTANILLA, M. & SAVIRÓN, J. M. 1988*a* Velocity measurements in convective flows by particle image velocimetry using a low power laser. *Opt. Engng* **27**, 641–649.

ARROYO, M. P., YONTE, T., QUINTANILLA, M. & SAVIRÓN, J. M. 1988*b* Particle image velocimetry in Rayleigh–Bénard convection: photographs with high number of exposures. *Opt. Lasers Engng* **9**, 295–396.

ARROYO, M. P., YONTE, T., QUINTANILLA, M. & SAVIRÓN, J. M. 1988*c* Three-dimensional study of the Rayleigh–Bénard convection by particle image velocimetry measurements. *LIA* **67**, ICALEO, 187–195.

BERGÉ, P. 1981 Rayleigh–Bénard convection in high Prandtl number fluid. In *Chaos and Order in Nature* (ed. H. Haken), pp. 14–24. Springer.

BERGÉ, P. & DUBOIS, M. 1984 Rayleigh–Bénard convection. *Cont. Phys.* **25**, 535–582.

BUHLER, K., KIRCHARTZ, K. R. & OERTEL, H. 1979 Steady convection in a horizontal fluid layer. *Acta Mech.* **31**, 155–171.

BUSSE, F. H. 1981 Transition to turbulence in Rayleigh–Bénard convection. In *Hydrodynamic Instabilities and the Transition to Turbulence* (eds H. L. Swinney & J. P. Gollub), pp. 97–137. Springer.

CHANDRASEKHAR, S. 1961 *Hydrodynamic and Hydromagnetic Stability*. Clarendon.

CHARLSON, G. S. & SANI, R. L. 1970 Thermoconvective instability in a bounded cylindrical fluid layer. *Intl J. Heat and Mass Transfer* **13**, 1479–1496.

DAVIS, S. H. 1967 Convection in a box: linear theory. *J. Fluid Mech.* **30**, 465–478.

DAVIS, S. H. 1968 Convection in a box: on the dependence of preferred wavenumber upon the Rayleigh number at finite amplitude. *J. Fluid Mech.* **32**, 619–624.

DUBOIS, M. 1981 Experimental aspects of the transition to turbulence in Rayleigh–Bénard convection. In *Stability of Thermal Systems* (eds J. Casas-Vasquez & G. Lebon), pp. 177–191. Springer.

DUBOIS, M. & BERGÉ, P. 1978 Experimental study of the velocity field in Rayleigh–Bénard convection. *J. Fluid Mech.* **85**, 641–653.

DUBOIS, M. & BERGÉ, P. 1981 Instabilities de couche limite dans un fluide en convection. Evolution vers la turbulence. *J. Phys. Paris* **42**, 167–174.

FRICK, H. & CLEVER, R. M. 1982 The influence of sidewalls on finite amplitude convection in a layer heated from below. *J. Fluid Mech.* **114**, 467–480.

GOLLUB, J. P. & BENSON, S. V. 1980 Many routes to turbulent convection. *J. Fluid Mech.* **100**, 449–470.

GOLLUB, J. P., MCCARRIAR, A. R. & STEINMANN, J. F. 1982 Convective pattern evolution and secondary instabilities. *J. Fluid Mech.* **125**, 259–281.

KOSTER, J. N., EHRARD, P. & MULLER, V. 1986 Nonsteady end effects in Hele-Shaw cells. *Phys. Rev. Lett.* **56**, 1802–1804.

MEYNART, R. 1983 Instantaneous velocity field measurements in unsteady gas flow by speckle velocimetry. *App. Opt.* **22**, 535–540.

NORMAND, C., POMEAU, Y. & VELARDE, M. G. 1977 Convective instability: a physicist's approach. *Rev. Mod. Phys.* **49**, 581–624.

OERTEL, H. 1981 Thermal Instabilities. In *Convective Transport and Instability Phenomena* (eds J. Zierep & H. Oertel), pp. 3–24. Braun.

PICKERING, C. J. D. & HALLIWELL, N. A. 1986–87 Automatic analysis of Young's fringe in speckle photography and particle image velocimetry. *Opt. Lasers Engng* **7**, 227–242.

SCHLUTER, A., LORTZ, D. & BUSSE, F. 1965 On the stability of steady finite amplitude connection. *J. Fluid Mech.* **23**, 129–144.

SHORT, M. & WHIFFEN, M. C. 1987 The relationship between density and analysis methodology in particle imaging velocimetry. In *Laser Anemometry in Fluid Mechanics III* (eds R. J. Adrian D. F. G. Durao, F. Durst and J. H. Whitelaw). Ladoan.

STORK, K. & MULLER, V. 1972 Convection in boxes: experiments. *J. Fluid Mech.* **54**, 599–611.

ZIEREP, J. & OERTEL, H. 1981 *Convective Transport and Instability Phenomena*. Braun.